Journal of Biomedical Optics 20(7), 076017 (July 2015)

Optical properties of plasmon-resonant bare and silica-coated nanostars used for cell imaging

Olga Bibikova,[a,*] Alexey Popov,[a] Alexander Bykov,[a] Artur Prilepskii,[b] Matti Kinnunen,[a] Krisztian Kordas,[c] Vladimir Bogatyrev,[b,d] Nikolai Khlebtsov,[b,d] Seppo Vainio,[e] and Valery Tuchin[a,f,g]

[a]University of Oulu, Faculty of Information Technology and Electrical Engineering, Department of Electrical Engineering, Optoelectronics and Measurement Techniques Laboratory, 3 Erkki Koiso-Kanttilan katu, Oulu 90570, Finland
[b]Institute of Biochemistry and Physiology of Plants and Microorganisms, Russian Academy of Science, 13 Prospect Entuziastov, Saratov 410049, Russian Federation
[c]University of Oulu, Faculty of Information Technology and Electrical Engineering, Department of Electrical Engineering, Microelectronics and Materials Physics Laboratories, 3 Erkki Koiso-Kanttilan katu, Oulu 90570, Finland
[d]Saratov State University, Faculty of Nonlinear Processes, Corporate Department of Biophysics, 83 Astrakhanskaya, Saratov 410012, Russian Federation
[e]University of Oulu, Faculty of Biochemistry and Molecular Medicine, Oulu Center for Cell-Matrix Research, Laboratory of Developmental Biology, 5A Aapistie, Oulu 90220, Finland
[f]Saratov State University, Faculty of Physics, Department of Optics and Biophotonics, 83 Astrakhanskaya, Saratov 410012, Russian Federation
[g]Institute of Precise Mechanics and Control, Russian Academy of Sciences, 24 Rabochaya, Saratov 410028, Russian Federation

Abstract. We synthesized and characterized gold nanostars and their silica-coated derivatives with 7- to 50-nm shell thicknesses as contrast agents for optical imaging. The scattering and absorption coefficients of the nanoparticles (NPs) were estimated by means of collimated transmittance and diffuse reflectance/transmittance analyses. The contrasting properties of the nanostructures were studied in optical coherence tomography glass capillary imaging. The silica-coated nanostars with the thickest shell have higher scattering ability in comparison with bare nanostars. Viability assays confirmed weak *in vitro* toxicity of nanostructures at up to ~200-μg/mL concentrations. We showed real-time visualization of nanostars in both agarose and cultured cells by analyzing the backscattering signal using a conventional laser confocal microscope. The signal intensity detected from the silica-coated NPs was almost 1.5 times higher in comparison with bare nanostars. To the best of our knowledge, this is the first time that conventional laser confocal microscopy was applied in combined scattering and transmitted light modes to detect the backscattered signal of gold nanostars, which is useful for direct monitoring of the uptake, translocation, and accumulation of NPs in living cells. [DOI: 10.1117/1.JBO.20.7.076017]

Keywords: gold nanostars; gold-silica nanoparticles; scattering; absorption; confocal microscopy; optical coherence tomography; glass capillary imaging.

Paper 150180PR received Mar. 18, 2015; accepted for publication Jun. 26, 2015; published online Jul. 31, 2015.

1 Introduction

Theranostics (simultaneous diagnosis and therapy within a single protocol) of cancer is an emerging trend in nanobiotechnology, necessitating multifunctional nanoparticles (NPs) that combine therapeutic, diagnostic, and sensing abilities in a single nanostructure.[1–3] These nanostructures are often composed of core–shell type composites, where the plasmon-resonant core simultaneously functions as an optical label and a therapeutic agent. The silica shell covering the NP also has a number of roles. It can enhance cargo volume, surface area, and colloidal stability, and it can also improve size- and shape-dependent optical properties.[4,5] Branched and star-shaped gold NPs become perspective candidates for use as a plasmon-resonant core of nanocomposites (NCs) due to their strong absorption in the near-infrared (NIR) wavelength range, optimal for the "diagnostic/therapeutic window" with enhanced light penetration into biotissue. In addition, the strong electric field concentrated at their branches[6,7] enables applications such as surface-enhanced Raman spectroscopy,[8] photodynamic therapy,[9] targeted delivery optical imaging,[10,11] and photothermolysis.[12]

Integration of plasmon-resonant nanoparticles (PRNPs) into biomedical applications requires the ability to change their absorption and scattering properties and tune the position of the resonance peak and associated scattering and absorption for optimal use. Although some experimental data on the relationship between the absorption and scattering properties of nanospheres and nanoshells,[13,14] nanorods,[15,16] and nanocages[17] are available, the majority of studies are devoted to the absorption properties of plasmonic NPs. Despite their importance as contrast agents in biophotonics, scattering characteristics attract much less attention from researchers. Here, we focused on the scattering component of the spectrum, crucial for imaging applications such as dark-field and confocal microscopy or optical coherence tomography (OCT). The latter is a noninvasive technique based on low-coherence interferometry utilizing backscattered light for *in vivo* imaging of layered tissues, allowing for distinguishing between normal and pathological tissue and for monitoring changes in optical properties.[18,19] The excellent

*Address all correspondence to: Olga Bibikova, E-mail: olyabibikova@gmail.com

1083-3668/2015/$25.00

contrast properties of gold nanoshells with a silica core,[20] functionalized gold nanospheres,[21] nanorods,[22] and nanocages[23] for OCT skin imaging have been exploited and also modeled with Monte Carlo simulations.[24] The measured absorption cross section of nanocages appeared to be about fivefold larger compared with conventional dyes.[25] On the other hand, branched gold NPs were shown to amplify the signal in water and agarose tissue-mimicking phantoms even under excitation not matching the resonance peak of the particles.[26]

Due to the high scattering, NPs are attractive agents for visualizing living cells and the dynamic processes occurring in them by using optical imaging techniques such as confocal,[27] differential interference contrast,[28] and dark-field[29] microscopic techniques. It has recently been demonstrated how different microscopic techniques, including laser confocal microscopy, can provide useful information about particle localization and properties.[30] Along with the integration of plasmonic nanostructures into the biological field, the uptake and toxicity of gold NPs and their derivatives is an emerging topic of modern nanomedicine and nanobiotechnology.[31,32] The effect of NPs on living cells and interactions between living and inorganic matter are important factors that may limit their use in biomedical applications.[33] Although no interaction between gold NPs and hemoglobin was found,[34] PRNPs can bind to a variety of plasma proteins, leading to an adsorbed protein layer or "corona" that largely defines the biological identity of these particles.[35] However, to study the effect of NPs on living cells, standard cell lines, such as A-549, HeLa, and 3T3 cells, are usually applied.[36,37] A recent study showed that the morphological features and surface chemistry of NPs define their cellular translocation dynamics.[38] Since both intracellular translocation after uptake and accumulation of NPs in cells are of high importance, here we summarize and extend our recent results[39,40] on the synthesis, optical, and contrasting properties of nanostars (NSts) and their silica-shell-coated NCs as well as their toxicity based on colorimetric and fluorescent viability assay analyses. For the first time, the scattering and absorption coefficients of bare and silica-coated nanostars were separated by means of collimated transmittance and diffuse reflectance/transmittance analyses and compared with the scattering and absorption properties of bare (NSps) and silica-coated (NCSps) nanosphere suspensions. In addition, we applied conventional laser confocal microscopy in combined scattering and transmitted light modes to detect the backscattered signal of gold nanostars for real-time visualization of intracellular localization of nanostars on living cells.

2 Materials and Methods

2.1 *Chemicals*

Gold(III) chloride trihydrate ($HAuCl_4 \times 3H_2O$), trisodium citrate dihydrate ($C_6H_5O_7Na_3 \times 2H_2O$), 1 N HCl, L(+)-ascorbic acid (AA), tetraethyl orthosilicate (TEOS), sodium borohydride ($NaBH_4$), 3-(4,5-dimethylthiazol-2-yl)-2,5-diphenyltetrazolium bromide (MTT), poly(vinyl pyrrolidone) (PVP; Mw = 55,000), and silver nitrate ($AgNO_3$) were purchased from Sigma-Aldrich with the highest purity grade available. Absolute isopropyl alcohol (IPA; 99.99%), ammonium hydroxide NH_4OH (29.5%), Dulbecco's modified Eagle's medium (DMEM), agarose, and penicillin-streptomycin solution were purchased from Sigma-Aldrich. DMSO (ACS grade) was purchased from Amresco; Milli-Q water (18 MΩ-cm; Millipore) was used in all preparations.

2.2 *Nanoparticle Synthesis*

Nanostars were synthesized with a slightly modified seed-mediated growth method, as described by Yuan et al.[41] Gold nanospheres were used as seeds. The nanosphere solution was prepared by reducing $HAuCl_4$ with sodium citrate using Grabar's method.[42] To prepare 15- and 50-nm nanospheres, 4.5 and 2.1 mL of 1% sodium citrate, respectively, were added quickly to boiling 0.03% $HAuCl_4$ (50 mL), resulting in a change in solution color from pale yellow to deep orange-red (15-nm NSps) or pink-red (50-nm NSps). For nanostar synthesis, 10 μL of 1 M HCl and 100 μL of the 15-nm NSps solution were added to 10 mL of 0.25 mM $HAuCl_4$ water solution at room temperature under vigorous stirring. Subsequently, 100 μL of 2 mM $AgNO_3$ and 50 μL of 0.1 M AA were added. The solution was stirred for 30 s while its color turned from light red to dark gray. Immediately afterward, 250 μL of 0.36 mM PVP was added under gentle stirring. The solution was stirred for 15 min and centrifuged at a 7500 relative centrifugal force (RCF) in terms of acceleration (g) for 10 min twice. The solution was redispersed in 0.5 mL of water.

2.3 *Silica-Coating of Nanoparticles*

A method from elsewhere[43] was used to form a silica shell on PVP-covered nanostars and nanospheres. Under gentle stirring, 0.5 mL of the nanostars was added to 2.25 mL of IPA. Ninety microliters of a 30% aqueous ammonia solution and various amounts of TEOS (from 6.25 to 50 μL) were added to the solution under continuous stirring to synthesize silica-coated nanostars or nanospheres with different thicknesses of silica shells. The reaction was allowed to proceed for 30 min at room temperature. The resulting solution was washed three times by centrifugation at 6000 RCF and the colloids were finally redispersed in 2 mL of water.

2.4 *Characterization of Nanostructures*

The average size of the particles was obtained by analyzing transmission electron microscopy (TEM) images (LEO 912 OMEGA, energy-filtered transmission electron microscope operating at 120 kV). To prepare samples for TEM, one drop of 10-μL nanostructure water suspension was deposited onto a carbon-coated copper grid. Statistical calculations were performed using ImageJ free software. Extinction and absorption coefficients of suspensions of bare and silica-coated nanostars were estimated using a spectrophotometer system (Optronic Laboratories) with integrating spheres working in diffuse reflectance/transmittance and collimated transmittance regimes. The scattering and absorption coefficients were retrieved from the measurements by applying Beer's law.

2.5 *Optical Coherence Tomography Experiments*

A hyperion spectral-domain optical coherence tomograph (Thorlabs) operating at a 930-nm central wavelength with an axial (along the Z-axis) resolution of 5.8 μm and a lateral resolution of 8 μm (in air) was used for imaging of bare and silica-coated nanostars in a capillary. Aqueous colloidal suspensions of gold nanostars and composites with a concentration of 1 mg/mL were added into 200-μm-thick plane glass capillaries.

Two-dimensional images of the capillaries with the suspensions were recorded with the OCT system and later processed with MATLAB software.

2.6 *Cell Viability Test*

Cell viability was examined using two modalities: a fluorescent cell viability assay with propidium iodide (PI) and an MTT assay. HeLa cells (Biocenter Oulu, Finland) were maintained at 37°C and 5% CO_2 in a complete DMEM medium supplemented with 10% bovine serum, 1% penicillin–streptomycin.

For the fluorescent assay, cells at a concentration of 10^6 mL^{-1} were maintained in 48-well culture plates in 400 mL of medium and incubated overnight with NPs at final concentrations of 12.5, 25, 50, 100, 200, and 400 $\mu g/mL$. After incubation, PI water solution was added to the cells to form the final concentration of 3 $\mu g/mL$. The cells were stained for 20 min in the dark at 37°C. The fluorescence of cells with compromised membranes (and thus considered dead) was registered by an Olympus IX81 epifluorescent inverted microscope equipped with a TRITC 41002c filter cube (Chroma). The ratio of fluorescing cells to the total number of cells in the field of view was calculated. The number of live cells in the sample of pure cells was set at 100%. Each experiment was triplicated. Standard deviation was used as error estimation.

To determine the respiratory activity of cells after incubation with the NPs, an MTT test, as described by Nicks and Otto[44] with minor modifications, was performed. The cells were maintained in 96-well culture plates in 200 μL of medium and incubated overnight with nanostars and NCs at concentrations of 12.5, 25, 50, 100, 200, and 400 $\mu g/mL$ (6.25×10^4, 1.25×10^5, 2.5×10^5, 5×10^5, 10^6, 2×10^6 NPs/cell, correspondingly). A 100-μL MTT solution (5 mg/mL) was added to each well of the plate with cell suspensions and incubated for 1 h in the dark at 37°C in a humidified atmosphere with 5% CO_2. After incubation, the supernatant was removed and 100 μL of DMSO was added to each well. The precipitate was resuspended and incubated for 15 min in the dark at 37°C. The solution from each well was centrifuged at 12,000 RCF for 3 min. The resulting supernatant was placed in wells of a 96-well flat-bottomed plate; absorbance readings were obtained with a Power Wave microplate spectrophotometer (Bio-Tek Instruments) at a wavelength of 490 nm. The respiratory activity of the nonirradiated sample was set at 100%. Each experiment was repeated three times.

2.7 *Confocal Microscopy Experiments*

Backscattering of the nanostructures was investigated by conventional laser confocal microscopy for both agarose and living

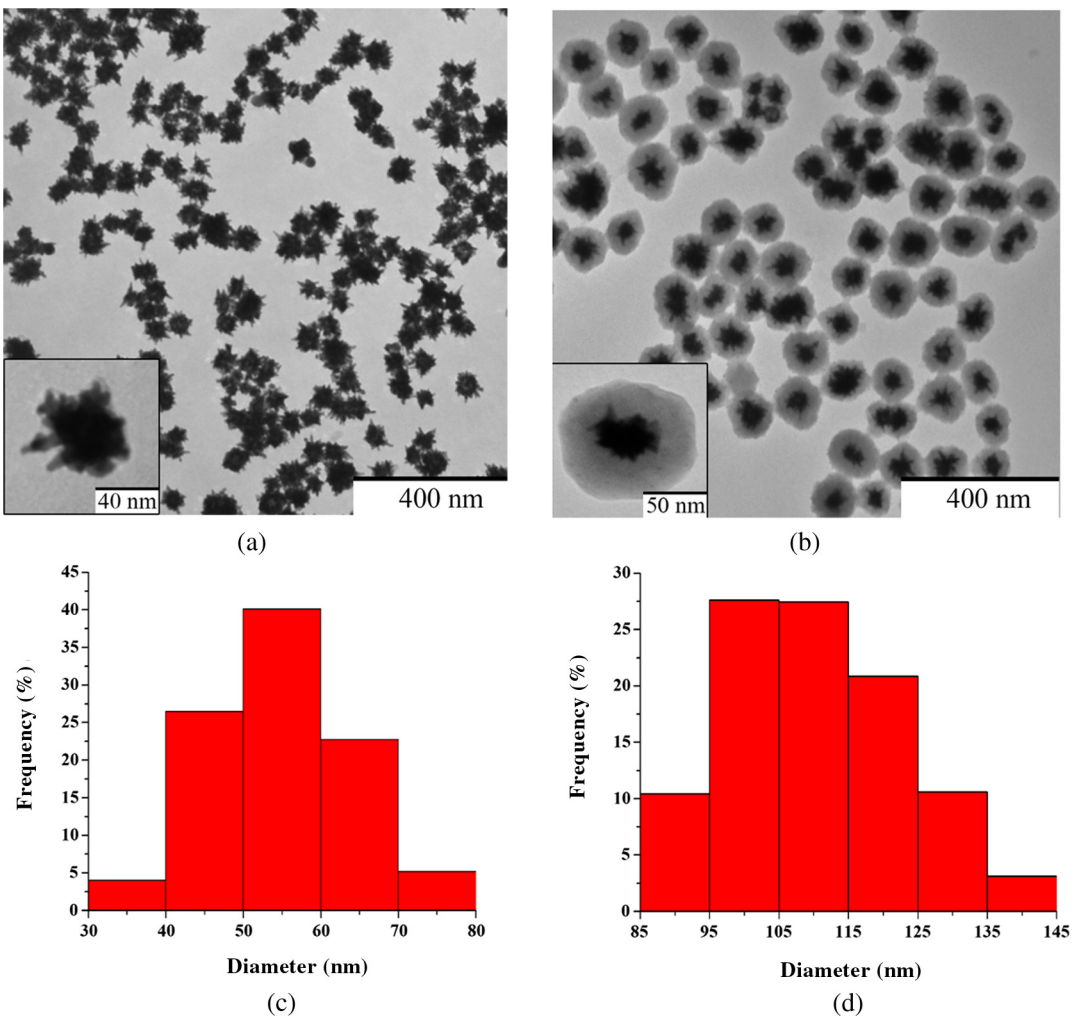

Fig. 1 Representative transmission electron microscopy images of (a) nanostars (NSts), (b) nanocomposites (NCs), and their corresponding size distribution diagrams (c and d).

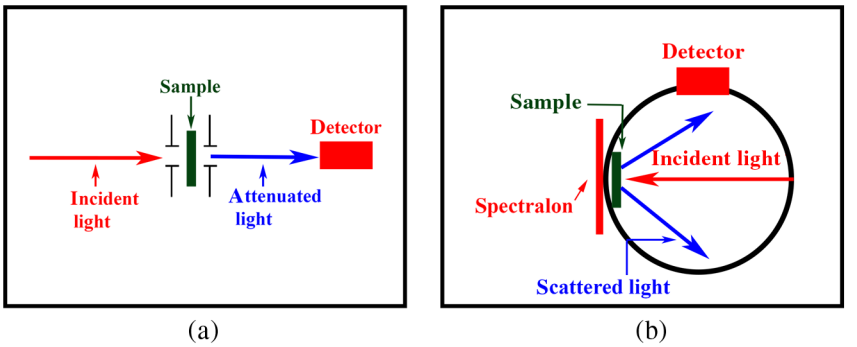

Fig. 2 Schemes for measuring (a) collimated transmission and (b) absorption.

cells. The samples were examined with a Zeiss LSM 780 laser scanning microscope with an EC Plan-Neofluar $10\times/0.3$ objective in a light scattering mode with an irradiating wavelength of 633 nm and a detection bandwidth of about 5 nm. To avoid saturation of the signal, the gain level was tuned to the same minimum value for all the samples. All the samples were scanned along the Z-direction in increments of 0.22 μm. Sixty-seven optical slices were analyzed from each sample. The thickness of the slices was the same (0.22 μm) for all the samples. The intensities of the signals were obtained for medial projections.

For agarose imaging, 20 μL of an aqueous colloidal solution of the NPs (stock concentration of the particles 1 mg/mL) was added to 100 μL of hot 1% aqueous agarose solution, stirred rapidly, loaded onto a precleaned glass, and covered with a cover glass, achieving the same layer thickness for each sample.

For *in vitro* imaging, the HeLa cells were maintained at 37°C and 5% CO_2 in a complete DMEM medium on a sterile microscopic cover glass and incubated overnight with gold nanostars and silica-coated gold nanostars at a gold concentration of 200 μg/mL. After incubation, the cover glasses with attached cells were put on microscopy glasses, sealed to avoid airing, and analyzed immediately.

3 Results and Discussion

3.1 *Synthesis and Characterization of Nanostructures*

Synthesis of gold nanostars is based on the reduction of chloroauric acid with AA and silver nitrate at room temperature on presynthesized gold nanospheres (diameter 15 nm) in aqueous

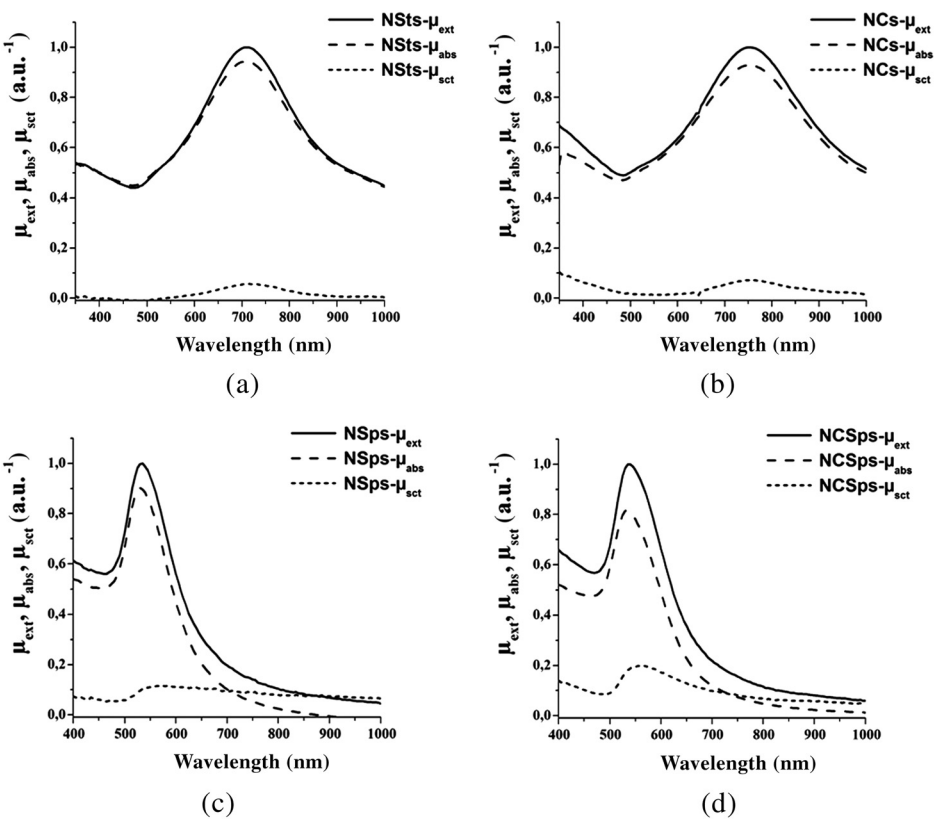

Fig. 3 Retrieved normalized spectra of extinction μ_{ext}, absorption μ_{abs}, and scattering μ_{sct} coefficients of (a) NSts, (b) NCs, (c) bare nanosphere suspensions, and (d) silica-coated (NCSps) suspensions.

media. Such nanostars, first developed by Vo-Dinh's research group,[41] are supposed to be beneficial for biological applications and optical imaging due to their biocompatible surfactant-free synthesis and because of the presence of thin sharp tips that can intensively interact with NIR excitation. The synthesis is simple; however, according to our experience, the nanostars are not stable enough. Even after functionalization by m-PEG-SH, as described in Fales' work,[9] irreversible aggregation was observed. To avoid significant aggregation, the nanostars were functionalized with PVP instead of PEG. A preliminary study of stabilization and the optical properties of nanostars are described by the authors elsewhere.[39] The PVP functionalization took 15 min, and the product proved to be stable for several months and allowed multiple centrifugation and redispersion cycles in different media.

The average diameter and shell thickness were obtained by analysis of TEM images of dried NP suspensions. To perform statistical analyses and calculations, we created a simple computation routine for image analysis using ImageJ software and estimated the dimensions of 500 particles on each given TEM image. Figure 1 shows representative TEM images of (a) NSts, (b) NCs, and (c and d) their corresponding size distribution diagrams.

The multibranched morphology with thin sharp tips is typical for seed-mediated grown nanostars. The size and number of branches of nanostars may be adjusted by changing the concentration of silver ions[41] and the ratio of auric chloride concentration to seed amount.[45–47] In a recent report by Khlebtsov et al., the size, morphology, and plasmon-resonant wavelength tunability of NSts were achieved by varying the initial size and concentration of seeds.[48] Here, NSts with an average tip-to-tip size of 55 ± 10 nm [Fig. 1(a)] were synthesized, similar to those reported by Khlebtsov et al.[48] and Yuan et al.[41] for NSts grown on seeds 15 nm in diameter. The silica shells of the nanostars were synthesized following the method depicted by Khlebtsov et al.[43] Shell thickness can simply be varied by changing the TEOS concentration and reaction time. Here, the amount of TEOS was 10 μL. The final silica-coated nanostars have an average size of 105 ± 16 nm with a shell thickness of about 25 ± 6 nm [Fig. 1(b)].

The absorption and scattering behaviors of PRNP suspensions define their applicability for biomedical optics; thus, both properties were measured for different types of particles with integrating spheres[49] and by OCT.[50] He et al.[51] used a monochromatic laser beam passing through the sample medium and then measured the absolute scattered energy within a small solid angle, and the total absolute scattering losses were finally obtained by integration over a 4π solid angle. Bogatyrev et al.[52] used a collimated light beam passing through the sample and measured the scattering spectrum along the 90 deg direction. Here, we apply a spectrophotometer with integrating spheres in a collimated transmittance and diffuse reflectance/transmittance configuration to estimate the scattering and absorption coefficients of our nanostructure suspensions (Fig. 2).

Under usual conditions, a spectrophotometer can be conveniently used to measure the collimated transmission of a

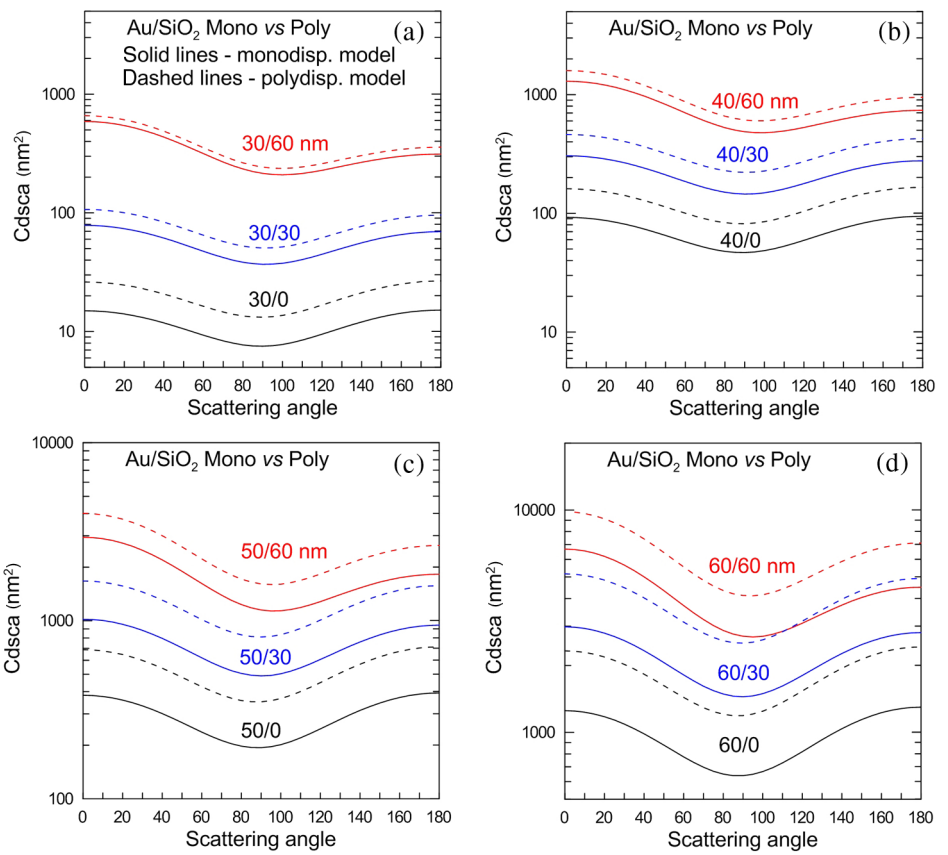

Fig. 4 Mie calculations of differential scattering cross sections (Cdsca) of bare 30-, 40-, 50-, and 60-nm gold NPs and silica-coated NPs with a 30-nm or 60-nm silica shell. The calculations were done for both monodisperse (solid lines) and polydisperse (dashed lines) models. Standard Gaussian distribution with the normalized standard deviation = 0.3 was used for polydisperse model.

suspension as a function of wavelength and to finally obtain the extinction spectrum of the sample. In this case, the extinction coefficient μ_t can be calculated as

$$\mu_t = -\frac{\ln(T_c)}{l}, \tag{1}$$

where T_c is the measured collimated transmittance and l is the cuvette's internal thickness (path length). The measured extinction coefficient is the sum of the absorption and scattering coefficients, which cannot be retrieved without further analysis.

To measure T_R, which is the sum of total transmittance T and reflectance R, we used an integrating sphere equipped with Spectralon™ (Labsphere, United States). Spectralon™ plays the role of a diffuse mirror due to its high reflectance, which is generally more than 95% for a wavelength range from 400 to 2500 nm.[53] Since the light passes the double optical path within a sample, the absorption coefficient μ_a is

$$\mu_a = -\frac{\ln(T_R)}{2l}. \tag{2}$$

Based on the above-mentioned equations, we can calculate the scattering coefficient as $\mu_s = \mu_t - \mu_a$. Figure 3 shows the retrieved extinction, absorption, and scattering coefficients of suspensions of bare and silica-coated nanostars [NSts, Fig. 3(a) and NCs, Fig. 3(b)], with initial and silica-coated 50-nm nanospheres [NSps, Fig. 3(c) and NCSps, Fig. 3(d)] given for comparison. For NCs and NCSps, the silica shell thicknesses were 25 ± 6 nm and 31 ± 7 nm, respectively.

According to the measured spectral data, the contribution of the scattering component to extinction is rather small, in line with

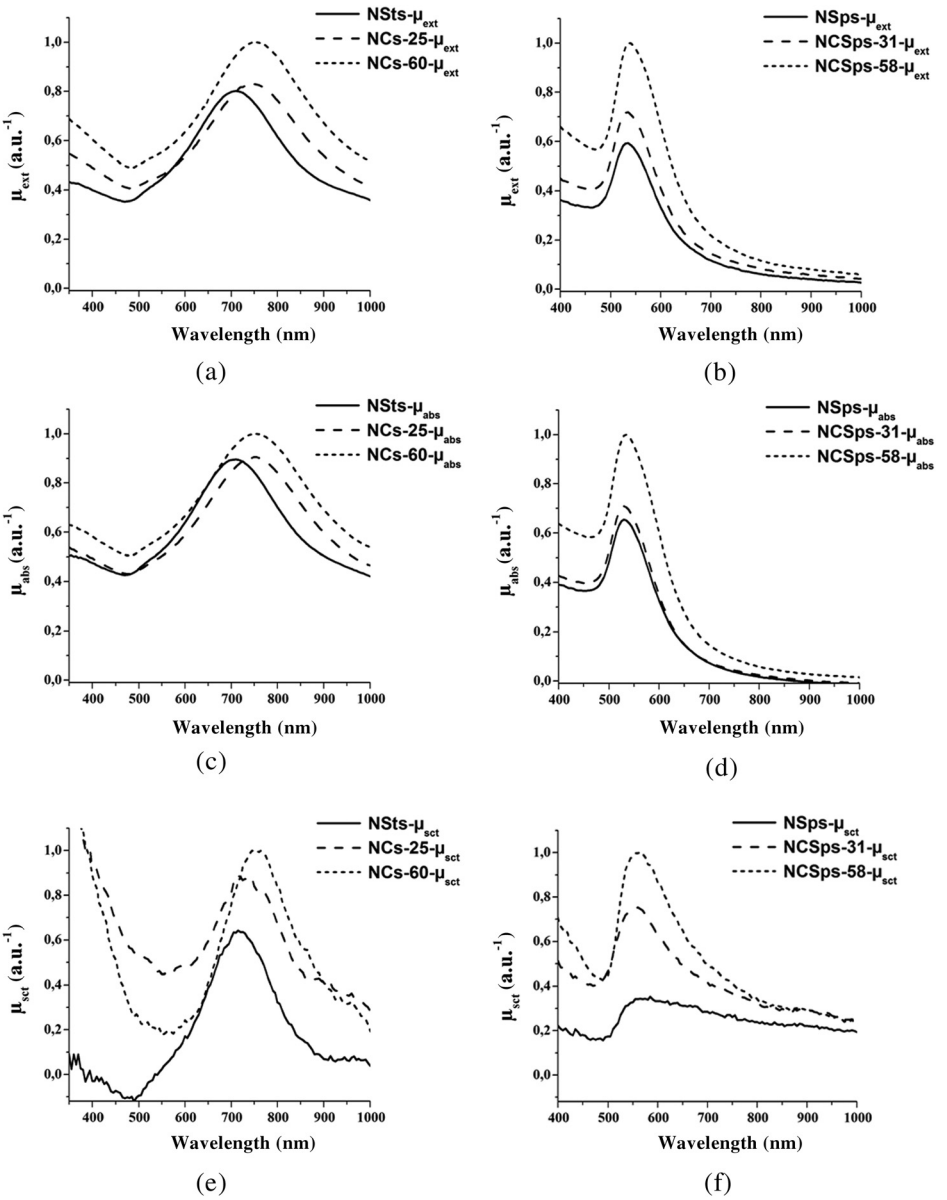

Fig. 5 Normalized spectra of extinction coefficients for suspensions of nanostars and their derivatives; (b) nanospheres and their derivatives; (c) spectra of absorption coefficients of nanostars and their derivatives; (d) nanospheres and their derivatives; (e) spectra of scattering coefficients of nanostars and their derivatives; and (f) nanospheres and their derivatives.

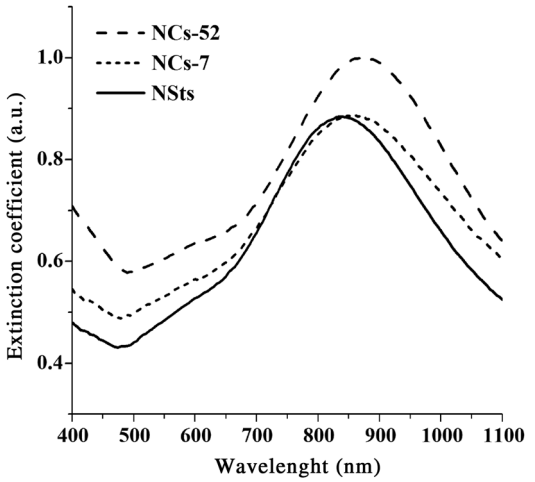

Fig. 6 Spectra of extinction coefficients of nanostars and nanocomposites with different silica shell thicknesses. Adapted from Ref. 40.

data reported for nanocages and nanorods of comparable size.[17] Since the scattering (Rayleigh) and absorption coefficients scale with particle size as[54] $\mu_s \sim r^6$ and $\mu_a \sim r^3$, larger nanostars scatter light stronger and are better suited for optical applications where the scattering intensity is critical. The stronger scattering ability of silica-coated nanostars can be theoretically explained by the use of nanospheres as a model, since similar scattering is an indicator of both NP types. Let us consider a simple two-layer model for gold nanospheres covered with a silica shell. Mie calculations (Fig. 4) for 30-, 40-, 50-, and 60-nm gold NPs show that silica coating in 30- and 60-nm layers results in a significant increase in differential scattering cross section in both forward and backward directions, whereas the scattering indicatrix retain their dipolar (Rayleigh) character. Physically, this enhanced scattering is explained by larger particle volume and, as a result, by large polarizability of composite particles. To the first approximation, the scattering intensity is proportional to the particle volume. As an example, after coating 60-nm Au particles with a 30-nm silica shell, the particle volume and scattering intensity roughly increased eight times.

Figure 5 depicts separate normalized spectra of the extinction, absorption, and scattering coefficients of NP suspensions for a convenient comparison of their absorption and scattering contributions to the total extinction of bare and coated NPs. The average diameters of NSts and NSps were 55 ± 10 and 50 ± 7 nm, respectively; the silica shell thicknesses of coated NSts were 25 nm (NCs-25) and 60 nm (NCs-60); and the silica shell thicknesses of coated nanospheres were 31 nm (NCSps-31) and 58 nm (NCSps-58).

The red shift of the spectral bands and the increase in the extinction value after silica-coating are well-known effects, associated with the change in the effective refractive index of the medium around the gold cores, demonstrated by experiments[9,55,56] and also explained by theoretical models.[57,58] The dependence of the plasmon-resonant peak on the dielectric environment for different types of PRNPs was investigated theoretically and experimentally. Our results, in good agreement with previous reports, show the expected red shift for the coated particles.

3.2 *Optical Coherence Tomography Experiments*

Evaluation of the scattering properties of nanostars and their core–shell structures from OCT experiments was the next stage of our study. Bare (NSts) and silica-coated nanostars with shell thicknesses of 7 nm (NCs-7) and 52 nm (NCs-52) were synthesized, resulting in particles with an average diameter of 51 ± 7 nm for NSts; 64 ± 10 nm for NCs-7; and 155 ± 20 nm for NC_S-52. Figure 6 depicts the normalized spectra of the obtained suspensions.

In addition, the results provide experimental evidence of the dependence of the shift on coating thickness (20 nm for NCs-7 and 30 nm for NCs-52 related to the uncoated nanostars).

A preliminary study on using nanostars for enhancement of the OCT image contrast of water flow in glass capillaries was demonstrated by the authors earlier.[40] The plasmon resonance maximum of the nanostructures (840 to 870 nm) is close to the emission spectrum of our superluminescent diode light source with the central wavelength of 930 nm and spectral bandwidth of 100 nm employed in the OCT system. Briefly, we concentrated the suspensions of NSts, NCs-7, and NCs-52 40 times in comparison with as-prepared solutions. Figure 7 shows the OCT images of capillary cross section with NP suspensions of NSts (a), NCs-7 (b), and NCs-52 (c). The scattering medium in the middle of the image is the NP suspension, and the brighter blue color corresponds to the stronger OCT (backward-reflected) signal.

In-depth distribution of the intensity registered from NP suspensions was retrieved from the measured data (Fig. 8). The slope of the in-depth OCT signals correlates with the scattering coefficient of the medium.[19] In the simplest case of single scattering, the scattering coefficient (or scattering cross section) could be directly calculated from the slope of the OCT signal using Beer's law. However, the multiple scattering significantly complicates this relation.[19,59]

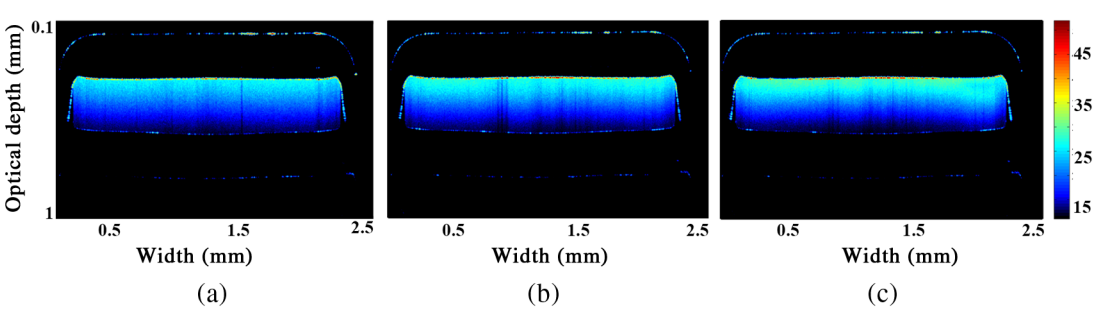

Fig. 7 Optical coherence tomography (OCT) images of capillary cross section with nanoparticle (NP) suspensions of (a) NSts, (b) NCs-7, and (c) NCs-52. Brighter color indicates higher scattering at $\lambda = 930$ nm. Inner capillary thickness is 200 μm. Adapted from Ref. 40.

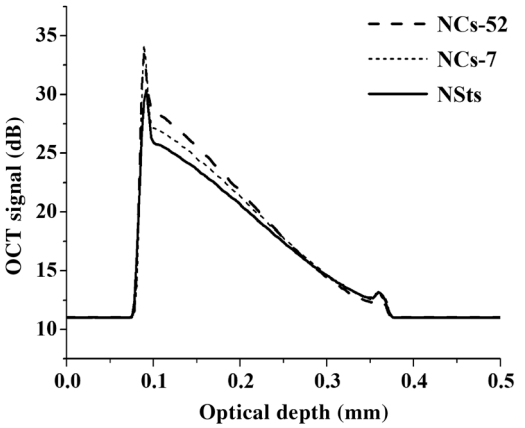

Fig. 8 In-depth distribution of the OCT signal over the capillary depth for the used NP suspensions. Adapted from Ref. 40.

In our case, the most intensive signal was registered from the silica-coated nanostars with the thickest silica shell. The spike on the left of all the curves is due to the glass–liquid interface. The backward scattering of the silica-coated nanostars, especially those with the thickest shell, is higher than the intensity of the signal from bare nanostars, which is in good agreement with previous reports[26] and measured spectral data (see Fig. 4) showing signal enhancement of branched gold NPs in OCT imaging in water and agarose gel. It should be noted that the red shift of NCs plasmon resonance maximum closer to the OCT instrumental wavelength increases the intensity of the OCT signal, which makes the NCs promising contrast agents for OCT. In addition, the use of larger nanostars for better correspondence of the plasmon-resonant wavelength with the emission band of OCT will be the subject of further studies.

3.3 *Confocal Microscopy Experiments*

For real-time visualization of the prepared NPs (NSts and NCs-52), the backscattered signal obtained with a conventional laser confocal microscope was analyzed in both agarose and cultured cells. To detect PRNPs' backscattering by reflectance confocal microscopy, we superimposed the signal detection band with the excitation laser wavelength (633 nm) and reduced the laser power and photomultiplier voltage to minimize the parasitic backscattered signal (background) from agarose gel or cell organelles. The choice of an excitation laser wavelength of 633 nm is conditioned by instrument characteristics; therefore, the wide plasmon-resonant peak of nanostars allows one to still use it as a contrast label for confocal microscopy at this wavelength. For the bulk solution experiment, NSts and NCs-52 were mixed with high-density agarose gel to avoid Brownian motion of the nanostructures before the suspensions were applied onto microscopy slides. Scattering intensity was evaluated and statistical measurements (mean intensity and standard deviation) were calculated using a ZEN software (Carl Zeiss, Germany) application in a histogram view. First, images of the samples' maximum intensity projection were obtained. Then the images were directly converted into binary images through a threshold. The binary image reveals whether a group of pixels in the image is recognized as a scattering spot. Finally, the intensity peak of each scattering spot was calculated and histograms of the intensity distribution were depicted. The whole process was realized in a ZEN black edition program. In Fig. 9, one can observe differences between the intensities of bare (a) and silica-coated nanostars (b) scattered signals. The silica-coated NPs have a higher scattering ability in comparison with bare nanostars, in agreement with the results obtained by OCT experiments. Relatively, large bright spots presented on the images may be caused by PRNPs' polydispersity (the scattering intensity is proportional to the particle volume, as shown earlier).

3.4 *Cell Studies*

To demonstrate the applicability of bare and silica-coated nanostars for *in vitro* experiments, we examined the influence of nanostructures at various concentrations on a HeLa cell line using two modalities: an MTT test and a fluorescent cell viability assay with PI as a stain for dead cells. The toxicity of PRNPs was shown to be dependent on their size, morphology, concentration, and surface properties.[60] Pernodet et al.[61] investigated *in vitro* the influence of gold nanospheres on cell activity at concentrations of 200, 400, 600, and 800 μg/mL. The high concentrations of NPs were toxic, since they penetrated through cell membranes and accumulated in vacuoles, affecting motility of the cells and their proliferative and adhesive abilities. An absence of toxicity has been shown by MTT assay for nanospheres up to a maximum particle concentration of 100 μg/mL in several research papers.[62,63] Here, we investigated the

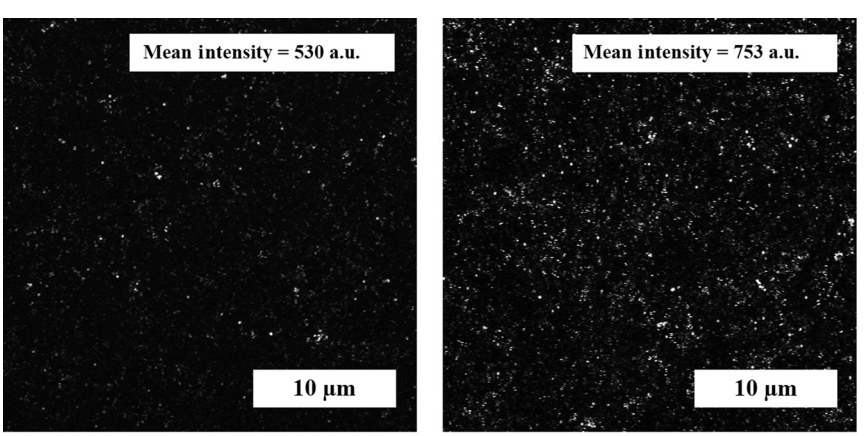

Fig. 9 Images of maximal intensity projection of the (a) NSts and (b) NCs-52.

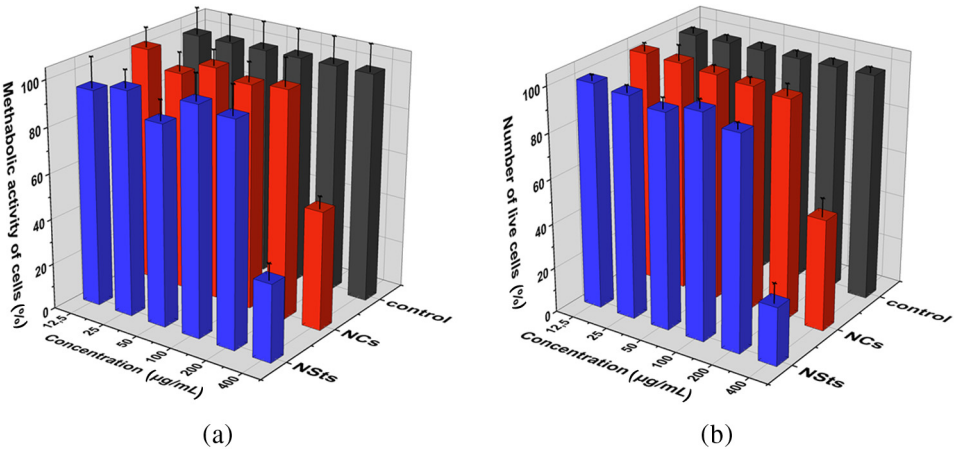

(a) (b)

Fig. 10 Cytotoxicity of silica-coated gold nanostars at different concentrations evaluated by (a) 3-(4,5-dimethylthiazol-2-yl)-2,5-diphenyltetrazolium bromide assay and (b) fluorescent cell viability assay with propidium iodide.

toxicity of NPs at concentrations of 12.5, 25, 50, 100, 200, and 400 μg/mL or 6.25×10^4, 1.25×10^5, 2.5×10^5, 5×10^5, 10^6, 2×10^6 NPs/cell, correspondingly. According to our results, all types of NPs have a significant impact on the metabolic activity of cells (about a 56% decrease in activity for NSts and about 44% for NCs) at a final concentration of gold equal to 400 μg/mL [Fig. 10(a)]. Smaller concentrations of NPs are harmless to the investigated cells when the differences in the values are within the standard deviation. Staining experiments using PI confirm the nontoxicity of silica-coated NSts and NCs up to a concentration of 200 μg/mL [Fig. 10(b)]. Similarly to the observations with the MTT assay, the amount of live cells decreased by 74% for NSts and by 50% for NCs in the case of a NP concentration of 400 μg/mL. Thus, the safe concentration of NPs used for real applications, e.g., cell imaging, should not exceed 200 μg/mL. It should be noted that due to the complexity and nonlinearity of biological systems such as living cells, the limited nontoxic concentration can vary up to five times, as was demonstrated in our previous study.[39] In Ref. 40, we indicate concentrations of gold in stock solutions added to the cell medium.

Interestingly, the relatively spherical NCs showed a similar effect on cell viability as the nanostars with their sharp tips, which can be explained by the difference in the size and morphology of the nanostructures. It has recently been shown that NPs with sharp corners and edges can break endosomal membranes and reside in the cytoplasm for a long time, disrupting cellular organelles and leading to increased cytotoxicity. Spherical NPs, in contrast, remain in endosomes after endocytosis, evolve with endosome maturation, and can be easily excreted via exocytosis.[64]

For intracellular experiments with confocal microscopy, we selected NSts as scattering particles and HeLa cells as model objects. Figure 11 shows images of living cells incubated with nanostars in (a) scattering, (b) transmitted, and (c) combined regimes. The difficulty of localizing the scattering NPs is due to the strong scattering interference of cells and their organelles, resulting in parasitic background illumination from the sample. Therefore, it is preferable to simultaneously observe cells in scattering and transmitted illumination modes.

Real-time visualization of living cells incubated with gold nanostructures allows monitoring of PRNP uptake and localization and focuses on the influence of plasmonic particles and complexes on cells, necessary for biomedical applications.

4 Conclusion

In summary, gold nanostars and silica-coated core–shell NPs with different coating thicknesses were synthesized and characterized to assess their plasmon resonance and scattering properties, particularly important for applications in theranostics. We

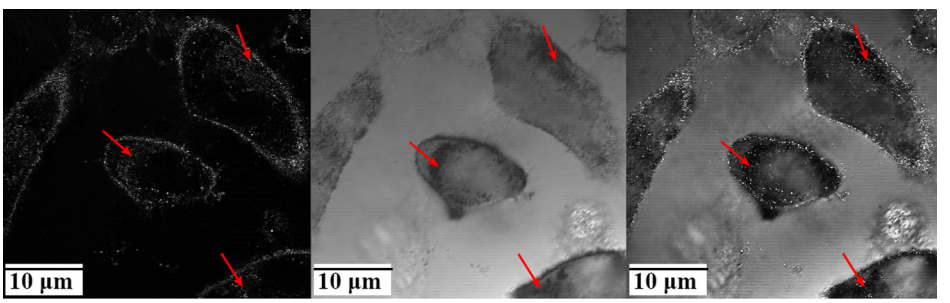

(a) (b) (c)

Fig. 11 (a) Medial slides of living cells incubated with NSts obtained in scattering mode, (b) transmission light mode and (c) combined regimes. The nanostructures are concentrated inside the cells (red arrows) and seen as bright/dark dots in the scattering/transmission light modes, respectively.

pioneered optical characterization of the gold nanostructures by decomposition of the attenuation into scattering and absorption. Both scattering and absorption were evaluated by using collimated transmittance and diffuse reflectance/transmittance measurements. The higher scattering properties of the silica-shell-coated NPs were exploited in OCT imaging of capillaries and also in reflectance confocal microscopy experiments in living cells. Nontoxicity of the investigated nanostructures, at least up to 200 μg/mL, is suggested by colorimetric and fluorescent cell viability assays.

To the best of our knowledge, this is the first time conventional laser confocal microscopy was applied in combined scattering and transmitted light modes to detect the backscattered signal of gold nanostars, which is useful for direct real-time observation of NP uptake and localization by living cells. The absence of potentially toxic fluorescent dyes in the samples enables focusing on the influence of plasmonic nanostructures exclusively, particularly important for biomedical and theranostics applications.

Acknowledgments

This research was supported by Infotech Oulu Graduate School and the Academy of Finland project 277697. We also acknowledge the support from BM1205 COST Action, the Government of the Russian Federation (Grant No. 14.Z50.31.0004 to support scientific research projects implemented under the supervision of leading scientists), and the Russian Presidential Grant NSh-703.2014.2. The work by NGK and VAB was supported by the Russian Scientific Foundation (Project No. 14-13-01167). We thank I. Skovorodkin and V.-P. Ronkainen for the collaborative work described in this paper.

References

1. B. Sumer and J. Gao, "Theranostic nanomedicine for cancer," *Nanomedicine* **3**(2), 137–140 (2008).
2. L. A. Dykman and N. G. Khlebtsov, "Gold nanoparticles in biomedical applications: recent advances and perspectives," *Chem. Soc. Rev.* **41**(6), 2256–2282 (2012).
3. A. P. Popov, A. V. Priezzhev, and R. Myllylä, "Optimal sizes of gold nanoparticles for laser treatment of tumors," *Proc. SPIE* **6534**, 65343K (2007).
4. B. Khlebtsov et al., "Nanocomposites containing silica-coated gold-silver nanocages and Yb-2, 4-dimethoxyhematoporphyrin: multifunctional capability of IR-luminescence detection, photosensitization, and photothermolysis," *ACS Nano* **5**(9), 7077–7089 (2011).
5. S. H. Cheng et al., "Tri-functionalization of mesoporous silica nanoparticles for comprehensive cancer theranostics—the trio of imaging, targeting and therapy," *J. Mater. Chem.* **20**(29), 6149–6157 (2010).
6. A. Guerrero-Martínez et al., "Nanostars shine bright for you," *Curr. Opin. Colloid Interface Sci.* **16**(2), 118–127 (2011).
7. C. L. Nehl, H. W. Liao, and J. H. Hafner, "Optical properties of star-shaped gold nanoparticles," *Nano Lett.* **6**, 683–688 (2006).
8. C. Hrelescu et al., "Single gold nanostars enhance raman scattering," *Appl. Phys. Lett.* **94**(15), 153113–153116 (2009).
9. A. M. Fales, H. Yuan, and T. Vo-Dinh, "Silica-coated gold nanostars for combined surface-enhanced Raman Scattering (SERS) detection and singlet-oxygen generation: a potential nanoplatform for theranostics," *Langmuir* **27**(19), 12186–12190 (2011).
10. E. Hutter et al., "Microglial response to gold nanoparticles," *ACS Nano* **4**(5), 2595–2606 (2010).
11. D. H. M. Dam et al., "Direct observation of nanoparticle cancer cell nucleus interactions," *ACS Nano* **6**(4), 3318–3316 (2012).
12. H. Yuan et al., "*In vivo* particle tracking and photothermal ablation using plasmon-resonant gold nanostars," *Nanomedicine* **8**(8), 1355–1363 (2012).
13. V. A. Bogatyrev et al., "Measurement of mean size and evaluation of polydispersity of gold nanoparticles from spectra of optical absorption and scattering optics and spectroscopy," *Opt. Spectrosc.* **96**(1), 128–135, (2004).
14. C. Ungureanu et al., "Differential pathlength spectroscopy for the quantitation of optical properties of gold nanoparticles," *ACS Nano* **4**(7), 4081–4089 (2010).
15. G. S. He et al., "Scattering and absorption cross-section spectral measurements of gold nanorods in water," *J. Phys. Chem.* **114**(7), 2853–2860 (2010).
16. K. Park et al., "Engineering the optical properties of gold nanorods: independent tuning of surface plasmon energy, extinction coefficient, and scattering cross section," *J. Phys. Chem.* **118**(11), 5918–5926 (2014).
17. E. Chul Cho et al., "Measuring the optical absorption cross sections of Au-Ag nanocages and Au nanorods by photoacoustic imaging," *J. Phys. Chem.* **113**(21), 9023–9028 (2009).
18. M. Kinnunen and R. Myllylä, "Application of optical coherence tomography, pulsed photoacoustic technique, and time-of-flight technique to detect changes in the scattering properties of a tissue-simulating phantom," *J. Biomed. Opt.* **13**(2), 024005 (2008).
19. J. Kalkman et al., "Multiple scattering effects in Doppler optical coherence tomography of flowing blood," *Phys. Med. Biol.* **57**(7), 1907–1917 (2012).
20. A. M. Gobin et al. "Near-infrared resonant nanoshells for combined optical imaging and photothermal cancer therapy," *Nano Lett.* **7**(7), 1929–1934 (2007).
21. C. S. Kin et al., "Enhanced detection of early-stage oral cancer *in vivo* by optical coherence tomography using multimodal delivery of gold nanoparticles," *J. Biomed. Opt.* **14**(3), 034008 (2009).
22. A. L. Oldenburg et al., "Imaging gold nanorods in excised human breast carcinoma by spectroscopic optical coherence tomography," *J. Mater. Chem.* **19**(35), 6407–6411 (2009).
23. J. Cen et al., "Gold nanocages: bioconjugation and their potential use as optical imaging contrast agents," *Nano Lett.* **5**(3), 473–477 (2005).
24. E. V. Zagaynova et al., "Contrasting properties of gold nanoparticles for optical coherence tomography: phantom, *in vivo* studies and Monte Carlo simulation," *Phys. Med. Biol.* **53**(18), 4995–5009 (2008).
25. J. Chen et al., "Gold nanocages: engineering their structure for biomedical applications," *Adv. Mater.* **17**(18), 2255–2261 (2005).
26. Y. P. de Léon et al., "Contrast enhancement of optical coherence tomography images using branched gold nanoparticles," *J. Nanomater.* **9**, 571015 (2012).
27. K. Sokolov et al., "Real-time vital optical imaging of precancer using anti-epidermal growth factor receptor antibodies conjugated to gold nanoparticles." *Cancer Res.* **63**(9), 1999–2004 (2003).
28. G. Wang et al., "Optical imaging of non-fluorescent nanoparticle probes in live cells," *Analyst* **135**(2), 215–221 (2010).
29. S.-H. Wang et al., "Size-dependent endocytosis of gold nanoparticles studied by three-dimensional mapping of plasmonic scattering images," *J. Nanobiotechnol.* **8**(33), 33 (2010).
30. N. Khlebtsov et al., "Analytical and theranostic applications of gold nanoparticles and multifunctional nanocomposites," *Theranostics* **3**(12), 167–180 (2013).
31. L. A. Dykman and N. G. Khlebtsov, "Uptake of engineered gold nanoparticles into mammalian cells," *Chem. Rev.* **114**(2), 1258–1288 (2014).
32. D. B. Chithrani, "Intracellular uptake, transport, and processing of gold nanostructures," *Mol. Membr. Biol.* **27**(7), 299–311 (2010).
33. N. Lewinski, V. L. Colvin, and R. Drezek, "Cytotoxicity of nanoparticles," *Small* **4**(1), 26–49 (2008).
34. D. Drescher et al., "SERS reveals the specific interaction of silver and gold nanoparticles with hemoglobin and red blood cell components," *Phys. Chem.* **15**(15), 5364–5373 (2013).
35. S. H. D. P. Lacerda et al., "Interaction of gold nanoparticles with common human blood proteins," *ACS Nano* **4**(1), 365–379 (2010).
36. N. G. Khlebtsov and L. A. Dykman, "Biodistribution and toxicity of engineered gold nanoparticles: a review of *in vitro* and *in vivo* studies," *Chem. Soc. Rev.* **40**(3), 1647–1671 (2011).
37. B. D. Chithrani and W. C. W. Chan, "Elucidating the mechanism of cellular uptake and removal of protein-coated gold nanoparticles of different sizes and shapes," *Nano. Lett.* **7**(6), 1542–1550 (2007).

38. Z. Chu et al., "Unambiguous observation of shape effects on cellular fate of nanoparticles" *Sci. Rep.* **4**, 4495 (2014).
39. O. Bibikova et al., "Plasmon-resonant gold nanoparticles with variable morphology as optical labels and drug carriers for cytological research," *Proc. SPIE* **8801**, 880102 (2013).
40. O. Bibikova et al., "Gold nanostructures for OCT imaging of capillary flow," *Proc. SPIE* **9129**, 912930 (2014).
41. H. Yuan et al., "Gold nanostars: surfactant-free synthesis, 3D modelling, and two-photon photoluminescence imaging," *Nanotechnology* **23**(7), 075102 (2012).
42. K. C. Grabar et al., "Preparation and characterization of Au colloid monolayers," *Anal. Chem.* **67**(4), 735–743 (1995).
43. B. N. Khlebtsov et al., "Enhanced photoinactivation of Staphylococcus aureus with nanocomposites containing plasmonic particlesand hematoporphyrin," *J. Biophotonics* **6**(4), 338–351 (2013).
44. M. Niks and M. Otto, "Towards an optimized MTT assay" *J. Immunol. Meth.* **130**(1), 149–151 (1990).
45. C. G. Khoury and T. Vo-Dinh, "Gold nanostars for surface enhanced Raman scattering: synthesis, characterization and optimization," *J. Phys. Chem.* **112**(48), 18849–18859 (2008).
46. P. S. Kumar et al., "High-yield synthesis and optical response of gold nanostar," *Nanothechnology* **19**(1), 015606 (2008).
47. J. Xie et al., "The synthesis of SERS-active gold nanoflower tags for in vivo applications," *ACS Nano* **2**(12), 2473–2480 (2008).
48. B. Khlebtsov et al., "Improved size-tunable synthesis and SERS properties of Au nanostars," *J. Nanopart. Res.* **16**, 2623 (2014).
49. S. Tassan et al., "Remote sensing—a scientific vision for sustainable development," in *IEEE Geosci. Remote. Sens.*, Vol. 2, 825 (1997).
50. H. Cang et al., "Gold nanocages as contrast agents for spectroscopic optical coherence tomography," *Opt. Lett.* **30**(22), 3048–3050 (2005).
51. G. S. He et al., "Scattering and absorption cross-section spectral measurements of gold nanorods in water," *J. Phys. Chem.* **114**(7), 2853–2860 (2010).
52. V. A. Bogatyrev et al., "Measurement of mean size and evaluation of polydispersity of gold nanoparticles from spectra of optical absorption and scattering," *Opt. Spectrosc.* **96**(1), 128–135 (2004).
53. G. T. Georgi and J. J. Butler, "Long-term calibration monitoring of Spectralon diffusers BRDF in the air-ultraviolet," *Appl. Opt.* **46**(32), 7893 (2007).
54. R. Lakowicz, "Radiative decay engineering 5: metal-enhanced fluorescence and plasmon emission," *Anal. Biochem.* **337**(2), 171–194 (2005).
55. A. V. Alekseeva et al., "Gold nanorods: synthesis and optical properties," *Colloid J.* **68**(6), 661–678 (2006).
56. N. G. Khlebtsov, "Optics and biophotonics of nanoparticles with a plasmon resonance," *Quantum Electron.* **38**(6), 504–529 (2008).
57. N.G. Khlebtsov et al., "Two-layer model of colloidal gold bioconjugates and its application to the optimization of nanosensors," *Colloid J.* **65**(4), 508–517 (2003).
58. B. N. Khlebtsov et al., "A simple Mie-type model for silica-coated gold nanocages," *J. Quant. Spectrosc. Radiat. Transfer* **121**, 23–29 (2013).
59. A. V. Bykov, M. Yu. Kirillin, and A. V. Priezzhev, "Monte Carlo simulation of an optical coherence Doppler tomograph signal: the effect of the concentration of particles in a flow on the reconstructed velocity profile," *Quantum Electron.* **35**(2), 135–139 (2005).
60. N. Khlebtsov and L. Dykman, "Biodistribution and toxicity of engineered gold nanoparticles: a review of *in vitro* and *in vivo* studies," *Chem. Soc. Rev.* **40**(3), 1647–1671 (2011).
61. N. Pernodet et al., "Adverse effects of citrate/gold nanoparticles on human dermal fibroblasts," *Small* **2**(6), 766–773 (2006).
62. Y. Qu and X. Lu, "Aqueous synthesis of gold nanoparticles and their cytotoxicity in human dermal fibroblasts-fetal," *Biomed. Mater.* **4**(2), 025007 (2009).
63. D. Shenoy et al., "Surface functionalization of gold nanoparticles using hetero-bifunctional poly(ethylene glycol) spacer for intracellular tracking and delivery," *Int. J. Nanomed.* **1**(1), 51–58 (2006).
64. R. E. Yanes, "Involvement of lysosomal exocytosis in the excretion of mesoporous silica nanoparticles and enhancement of the drug delivery effect by exocytosis inhibition," *Small* **9**(5), 697–704 (2013).

Biographies for the authors are not available.